

# Optimizing the Quantum Confined Stark Effect in Nanorods for Single-Molecule Electrophysiology

*Yung Kuo<sup>1</sup>, Jack Li<sup>1</sup>, Noga Meir<sup>2</sup>, Xavier Michalet<sup>1</sup>, Emory Chan<sup>3</sup>, Dan Oron<sup>2</sup>, Shimon*

*Weiss<sup>1,4,5,6</sup> \**

1 Department of Chemistry and Biochemistry, University of California Los Angeles, Los Angeles, CA 90095

2 Weizmann Institute of Science, Rehovot 76100, Israel

3 The Molecular Foundry, Lawrence Berkeley National Laboratory, Berkeley, California, 94720

4 California NanoSystems Institute, University of California Los Angeles, Los Angeles, CA 90095

5 Department of Physiology, University of California Los Angeles, Los Angeles, CA 90095  
6 Department of Physics, Institute for Nanotechnology and Advanced Materials, Bar-Ilan University, Ramat-Gan, 52900, Israel

KEYWORDS Quantum confined Stark effect, quantum dots, membrane potential, single molecule

**ABSTRACT** We optimized the performance of quantum confined Stark effect (QCSE)-based voltage nanosensors. A high-throughput approach for single-particle QCSE characterization was developed and utilized to screen a library of such nanosensors. Type-II ZnSe/CdS seeded nanorods (synthesized by a robotic colloidal synthesizer) were found to have the best performance among the different nanosensors evaluated in this work. The degree of correlation between intensity changes and spectral changes of the exciton's emission under applied field was characterized. An upper limit for the temporal response of individual ZnSe/CdS nanorods to voltage modulation was characterized by high-throughput, high-temporal resolution intensity measurements using a novel photon-counting camera. The measured 3.5  $\mu$ s response time is limited by the voltage modulation electronics and represents  $\sim x 30$  times higher bandwidth than needed for recording an action potential in a neuron.

## 1. Introduction:

Nanoparticles (NPs) with extremely bright fluorescence have enabled new fields of biological and biophysical studies<sup>1, 2</sup>, such as single-particle imaging and tracking<sup>3, 4</sup>, single-particle sensors<sup>2, 5</sup>, and super-resolution microscopy<sup>6, 7</sup>. In particular, semiconductor quantum dots (QDs) have been used as biological probes in various applications, for example as labeling agents for long-term tracking of single molecules<sup>3</sup> and as intracellular sensors for temperature<sup>5, 8</sup>, pH<sup>9</sup>, etc. Within the past decade, QDs or nanorods (NRs) were also predicted theoretically and observed experimentally to report cellular membrane potential with exceptionally large sensitivities<sup>10-14</sup>. With the versatile capabilities already shown and with some advanced engineering, QDs / NRs have great potential to become next-generation voltage nanosensors that enables membrane potential imaging using single particles. In this work, we synthesized, characterized, and optimized QDs and NRs to exhibit enhanced quantum confined Stark effect (QCSE) using a dedicated high-throughput single-particle screening approach.

As neurons transmit signals via electrical impulses generated by membrane potential modulations, two approaches are traditionally taken to monitor neural activities: (i) direct electrical recording, or (ii) utilization of a sensor that transduces the electrical observables into other signals, such as fluorescence. Electrical monitoring involves the patch clamp technique or microelectrode arrays which are both highly invasive and not suitable for simultaneous recording from a large number of neuron cells for studying how neurons communicate within a network or from nanostructures in a neuron for studying local electrical events (due to the space constraint for the bulky electrodes). Many important brain functions such as transmission of signals, plasticity, learning, and memory<sup>15-18</sup> are facilitated by complex electrical and chemical events in tiny structures such as dendritic spines and synapses that are less than 1  $\mu\text{m}^3$  in volume<sup>19</sup> and are

extremely dynamic in shape and size<sup>20-22</sup>. Studying local electrical signals from such small volumes requires the development of bright and non-invasive probes that are nanometer in size and hence allowing for high spatial resolution recording. Optical sensors such as voltage-sensitive dyes (VSDs)<sup>23-26</sup> and genetically encoded voltage indicators (GEVIs)<sup>27-29</sup> are examples for the second approach. VSDs and GEVIs can report on changes in membrane potential via changes in their absorption / emission properties<sup>30</sup>. Despite the advances made with VSDs, GEVIs and their hybrids<sup>30-34</sup>, they cannot monitor electrical events on the nano-scale with single-molecule resolution. Additionally, both VSDs and GEVIs suffer from photobleaching, low voltage sensitivity, toxicity, and/or slow kinetics, and they perturb membrane capacitance.

While organic dyes and fluorescent proteins may be further improved in the future, nanoparticles (NPs) could offer alternatives. For example, nitrogen-vacancy centers in nanodiamonds could report action potentials (APs) in a giant axon of *M. infundibulum* (worm) via optical detection of magnetic resonance (ODMR) technique<sup>35</sup>. QDs can operate as voltage sensors via photo-induced electron transfer<sup>12, 36, 37</sup> or the quantum confined Stark effect (QCSE)<sup>10, 11, 14</sup>. The physical origin of the QCSE is in the separation of the confined photo-excited charges in the semiconductor QD or NR, creating a dipole that opposes the external electric field. This, in turn, leads to (red or blue) shifting of the absorption and emission edges that are accompanied by quantum yield (QY) and fluorescence lifetime changes according to the Fermi golden rule. Therefore, QDs or NRs with sizable QCSE (at room temperature) that are properly inserted into the cell membrane could report on changes in membrane potential via a spectral shift, a change in the emission intensity, and/or a change in the excited state lifetime. QCSE-based QDs / NRs voltage sensors could also offer several advantages over existing voltage sensors based on organic dyes, fluorescent proteins, or their hybrid: they (1) have high voltage sensitivity (quantified as

percent change in fluorescence intensity,  $\Delta F/F$ ), (2) exhibit large spectral shifts ( $\Delta\lambda$ ) enabling ratiometric detection, (3) exhibit changes in excited state lifetime (providing alternative detection scheme), (4) have high brightness affording single-particle detection and superresolution recording, (5) have a fast response time ( $\sim$ ns) based on QCSE, (6) have highly functionalizable surface, (7) have engineerable emission wavelength and quantum yield (QY), (8) have negligible photobleaching, and (9) have low cytotoxicity (after surface modification). With the extremely fast response time, QDs / NRs will be capable of reporting and resolving the APs, which not only have fast dynamics (sub-ms) but also present in a wide range of frequencies and waveforms, especially in mammalian brains<sup>38-43</sup>.

However, there are some challenges to overcome before QCSE-based QDs / NRs voltage sensors can achieve single-particle voltage imaging. First, the larger the QDs or the longer the NRs are, the larger is their polarizability and hence their voltage sensitivities<sup>10, 13</sup>. However, for proper membrane potential reporting, the QDs / NRs need to be functionalized and inserted into the 4-nm thick cell membrane. Therefore, optimization with regard to the trade-off between magnitude of the QCSE (dependent on NP's size and materials) vs. ease of membrane insertion (inversely dependent on NP's size) is required. Secondly, QDs / NRs synthesized by colloidal synthesis are inevitably poly-dispersed, especially when multiple materials or anisotropic growth (for NRs) are involved. The polydispersity among particles will introduce a large distribution in their voltage sensitivities, resulting in difficulties in evaluating the single-particle performance of these nanosensors using ensemble spectroscopic methods. These challenges need to be addressed *in vitro* first before attempting to utilize QDs / NRs as single-particle voltage nanosensors in live neurons.

In this work, we addressed these challenges in several steps. First, we synthesized type-II ZnSe seeded CdS NRs (in a dot-in-rod structure) with enhanced QCSE while maintaining small

dimensions. A type-II heterostructure increases charge separation by presenting spatially separated band energy minima for electrons and holes across the heterojunction and hence increases voltage sensitivity by QCSE without increasing the dimensions of NRs significantly. In addition, the dot-in-rod structure is often shown to be asymmetric, creating an asymmetric charge separation and linear dipole that screens the external field<sup>44</sup>. In previous theoretical works, type-II NRs were predicted to exhibit large voltage sensitivities<sup>12, 13</sup>, and NRs  $< 12$  nm were shown to have minimal difficulties in membrane insertion after surface functionalization<sup>14</sup>. To address the second challenge, we developed a single-particle high-throughput screening methodology, which enables iterative optimization of the synthesis. The screening was based on single-particle spectral shift ( $\Delta\lambda$ ) and relative intensity change ( $\Delta F/F$ ) observables and allowed for statistical evaluation of NR's properties. This approach required (i) the fabrication of thin film microelectrodes that “sandwiched” NRs or QDs to allow application of homogeneous electric field vertically; (ii) building a spectrally resolved wide-field single molecule microscope; (iii) implementing a code for automated data analysis. With this high-throughput *in vitro* screening approach, we compared the voltage sensitivities and screened various QDs and NRs of different material compositions (including doping), sizes, and band alignments and acquired sufficient single-particle statistics for their assessment. Short type-II NRs exhibited larger single-particle voltage sensitivity than longer type-I NRs, validating the concept of QCSE optimization by proper engineering of NP's composition and bandgap / hetero-interface alignment. This single-particle screen allowed us to systematically and iteratively improve and optimize the NRs synthesis, and improve homogeneity, quantum yield, and voltage sensitivity. The improved NRs exhibited voltage sensitivity, characterized by a up to 69% relative intensity change ( $\Delta F/F$ ) and a  $\sim 4.3$  nm spectral shift ( $\Delta\lambda$ ),

fast response time ( $< 3.5 \mu\text{s}$ , an upper bound set by the RC time constant of the voltage modulation electronics), and high brightness, affording facile single-particle detection.

## 2. Results:

### 2.1. Nanorod synthesis

Reaction parameters that allow precise control of anisotropic growth are critical for NRs of small size ( $\sim 10 \text{ nm}$ ) as studied here. Poor control would yield NRs with low aspect ratio (hence more symmetric and with reduced QCSE).

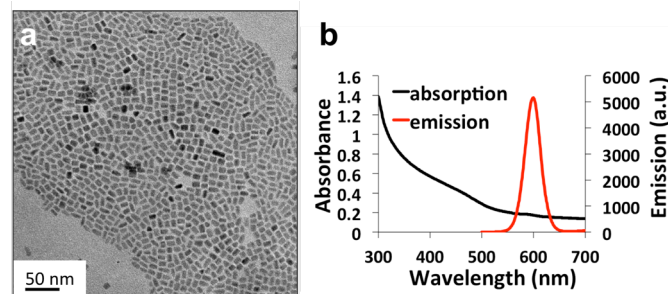


**Fig. 1:** ZnSe/CdS NRs synthesized on WANDA. (a) TEM image of NRs. (b) absorption and emission spectra of NR (in toluene).

Previous works reporting the synthesis of seeded ZnSe/CdS NRs focused on much longer NRs (40 nm to 100 nm)<sup>44, 45</sup>. Simply quenching the reaction after a short amount of time usually yielded polydisperse distributions in the length and width of the NRs. For voltage sensing, shorter NRs are required due to the difficulty to insert longer NRs ( $> 12 \text{ nm}$ ) into the membrane<sup>14</sup>. In order to determine optimal synthesis parameters to obtain shorter NRs with high aspect ratio, and to precisely control reaction parameters, we used a high-throughput robot (WANDA<sup>46</sup>) to systematically vary nanocrystal growth parameters and screen for NRs with aspect ratios greater than 1.5 and lengths less than 12 nm. Our  $\sim 12 \text{ nm}$  NR synthesis was based on a published procedure<sup>44</sup> with one modification: we used an alkanethiol in the place of trioctylphosphine sulfide (TOPS) as the S precursor to control the reaction kinetics and to slow down initial growth rate. Thiol precursors of different carbon chain length (from dodecanethiol to octadecanethiol) were

tested. The injection and growth temperatures respectively were optimized in multiple optimization runs, in order to achieve slower initial growth rate and hence obtain shorter NRs. The transmission electron microscopy (TEM) image and absorption and emission spectra of the batch of ZnSe/CdS NRs with minimal size distribution and high aspect ratios revealed by TEM are shown in Fig. 1. The synthesis was iteratively optimized using a series of screening assays including UV-VIS, TEM, and QCSE measurements (details shown below) to yield NRs with length  $< 12$  nm and aspect ratio  $> 1.5$  while maintaining a large QCSE responses. Particle size analysis of the best batch shown in Fig. 1 reports an average of  $11.6$  nm  $\pm 1.7$  nm (1 sigma from Gaussian fitting) for the long NR's axis and an average of  $6.8$  nm  $\pm 1.3$  nm (1 sigma from Gaussian fitting) for the short axis/diameter. The average aspect ratio was  $1.9 \pm 0.5$  (1 standard deviation) (see Fig. S1).

## 2.2. Set-up and protocol for high-throughput single-particle QCSE measurements

To characterize NRs' QCSE-induced spectral shift and intensity change (upon external field modulation) with sufficient statistical significance, a dedicated set-up, methodology, and analysis had to be developed. To apply electric field of magnitude similar to that generated by the depolarization phase of an AP, we followed the approach of a previous work<sup>36</sup> (with a few modifications) to fabricate microelectrode stacks using thin film depositions. The thin film electrodes "sandwiched" the NPs of interests and allowed application of homogeneous electric field while allowing imaging with a high numerical aperture (N.A.) objective. The stack was comprised, from bottom to top, of an indium tin oxide (ITO)-coated coverslip, SiO<sub>2</sub> for insulation, NPs of interest, polyvinylpyrrolidone (PVP), SiO<sub>2</sub> for insulation, and gold electrode (schematically shown in Fig. S2). The NPs in such devices were stable for several weeks and up to 2 months after

fabrication. NPs in older devices, such as lithographically-patterned electrodes, tended to rapidly photobleach, possibly due to oxidation by exposure to air. Also, as compared to the horizontal lithographically-patterned electrodes, the vertical stack device suffer significantly fewer catastrophic arc discharge or meltdown events<sup>11</sup>. This “sandwich device” can be fabricated with either a large NP density (for ensemble measurements) or with a smaller density (for single particle measurements) by controlling the dilution and spin-coating conditions. We use low concentration to test and optimize our NRs as single-particle voltage nanosensors. A dedicated wide-field and spectrally-resolved single molecule microscope (inspired by previous work<sup>47</sup>, Fig. S3) was designed (see Materials and Methods and supporting information for details). It allowed acquiring modulated spectra of hundreds of individual single NPs per measurement while applying alternating voltage from frame to frame. Briefly, the camera acquisition was synchronized to a modulated voltage source that was applied to the test device, creating an electric field alternating from 0 kV/cm ( $V_{\text{off}}$ ) to 400 kV/cm ( $V_{\text{on}}$ ) in consecutive frames. The fluorescence emitted by individual NRs were spectrally dispersed by a prism inserted in the detection path and imaged by a camera. Spin-coated fluorescent beads with known emission wavelengths were used for wavelength calibration (SI-4). Movies of 600 frames (300 modulations periods) were recorded for all samples.

To analyze the QCSE of single NRs, the spectrally dispersed point spread functions (PSFs) of individual NRs were selected from the mean frame of the entire movie using an algorithm for automatic PSF detection (described in SI-5), and the following analysis was performed only on the selected NRs. Wavelengths calibration for each pixel was performed according to the protocol described in SI-4, allowing the accurate extraction of the (calibrated) spectrum for each NR,

anywhere is the field-of-view. Thus, the spectrum, the integrated intensity, and the peak wavelength for each NR in each frame could be automatically derived.

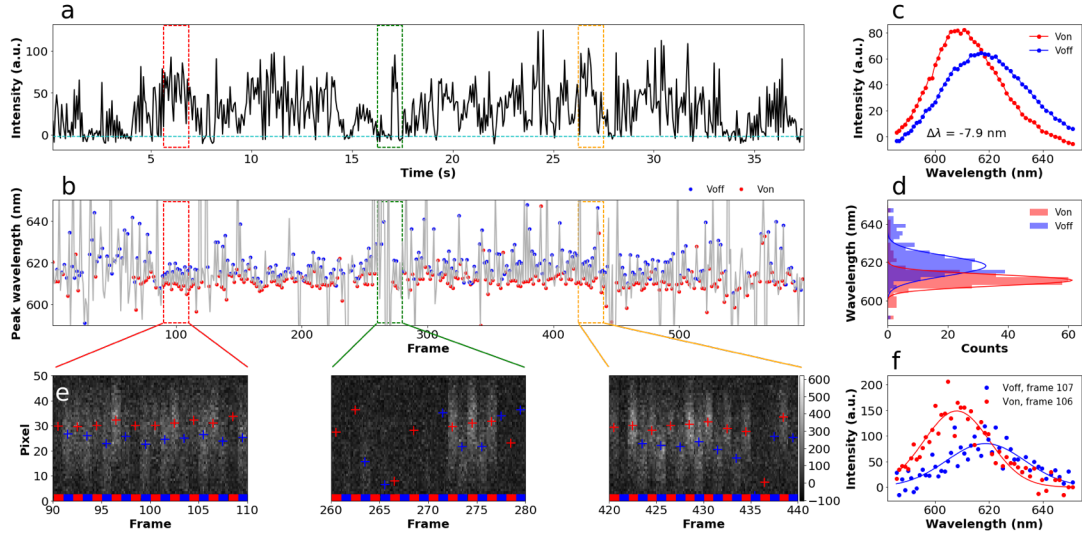


**Fig. 2:** An example for QCSE measurements of a single ZnSe/CdS NR. (a) Intensity trace and (b) spectral peak position trace as function of frames. (c) Averaged emission spectrum for V<sub>on</sub> (red) and V<sub>off</sub> (blue) frames that were above the blinking threshold (cyan dashed line in (a)). (d) Histograms of spectral peak positions from individual frames for V<sub>on</sub> (red) and V<sub>off</sub> (blue) frames that were above the blinking threshold (cyan dashed line in (a)). Fitting the two peak position distributions to Gaussian functions (red and blue lines for V<sub>on</sub> and V<sub>off</sub> histograms, respectively) showed that the centers were shifted by 7.5 nm, consistent with the result in (c). (e) Images of the prism-dispersed PSFs from 20 consecutive frames ('zoom-ins') at 3 different time periods of the background subtracted movie. The prism-dispersed PSFs from different frames are stacked side by side, with the blue and red segments marking the V<sub>off</sub> and V<sub>on</sub> frames, respectively. The peak positions are marked with red and blue '+'s for V<sub>on</sub> and V<sub>off</sub> frames, respectively. The clear 'up' and 'down' displacements between consecutive dispersed PSFs are strong evidences for spectral shifts (converted to nm by calibration procedure detailed in SI-4). The intensity of each pixel in (e) is shown in greyscale with the colorbar shown on the right. (f) Emission spectrum extracted from a single V<sub>on</sub> (red) and V<sub>off</sub> (blue) frame. The blue and red lines show the Gaussian fit to the spectrum for the V<sub>on</sub> and V<sub>off</sub> frame, respectively.

An example of a single ZnSe/CdS NR QCSE analysis is shown in Fig. 2. The intensity time trace and extracted spectral peak positions of a single NR are shown in Fig. 2a and 2b, respectively. The red and blue dots in Fig. 2b respectively highlight the spectral peak positions during frames with (V<sub>on</sub>) or without (V<sub>off</sub>) applied voltage. Clear fluctuations of intensity or peak wavelengths from frame to frame due to voltage modulation can be observed. This NR is an example of the NR sub-population that does not show clear 'on' and 'off' blinking states (Fig. S5-2a). While a cyan dashed line is provided as a guide to the eye to distinguish blinking states, this particular NR clearly shows the difficulty in determining blinking threshold, and therefore in Section 2-3, the "burst analysis" (details described in SI-5) was implemented for further analysis

without applying a blinking threshold to avoid the associated bias. The averaged emission intensity change ( $\Delta F/F$ ) and spectral shifts ( $\Delta\lambda$ ) are calculated using equations below:

$$\langle \Delta F/F \rangle = \frac{\langle F_j^{V_{on}} \rangle_{j=b_{on}} - \langle F_j^{V_{off}} \rangle_{j=b_{on}}}{\langle F_j^{V_{off}} \rangle_{j=b_{on}}} \quad \text{eq. (1)}$$

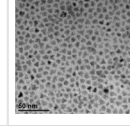
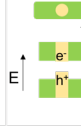
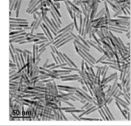
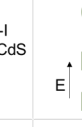
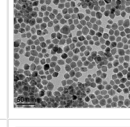
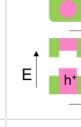
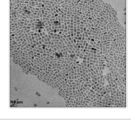
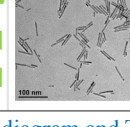
$$\langle \Delta\lambda \rangle = \left\langle \lambda_j^{V_{on}} \right\rangle_{j=b_{on}} - \left\langle \lambda_j^{V_{off}} \right\rangle_{j=b_{on}} \quad \text{eq. (2)}$$

where  $F$  is the fluorescence intensity and  $\lambda$  is the peak wavelength.  $V_{on}$  and  $V_{off}$  note the frames with ( $V_{on}$ ) or without ( $V_{off}$ ) applied voltage, respectively, and  $b_{on}$  notes the frame that has intensity above the blinking threshold. The  $\Delta F/F$  and  $\Delta\lambda$  resulting from QCSE shown in Fig. 2c are extracted from only the ‘on’ states, determining by the emission intensity higher than the cyan threshold. Fig. 2e shows the spectrally dispersed PSFs in 3 series of 20 consecutive frames corresponding to different time windows delimited by boxes in the time trace (Figs. 2a and 2b). They exhibit clear alternated spectral shifts in consecutive frames due to field modulation. The red and blue segments at the bottom of the panels mark the  $V_{on}$  and  $V_{off}$  frames. The frames missing clear dispersed PSFs in these panels (for example frame 260-271 in the second panel) indicate the blinking ‘off’ state. Fig. 2c shows that the averaged emission spectrum at 400 kV/cm is blue-shifted by 7.9 nm, the FWHM of the emission spectrum is narrowed by 6 nm (Fig. S5-2b), and the integrated intensity is increased by 9% ( $\Delta F/F$ ) with respect to the spectrum in the absence of applied field. This blue shift and increased intensity are consistent with the NR’s expected type-II band structure<sup>11,13</sup>. An example for a  $V_{on}$  and a  $V_{off}$  spectrum from one single frame and the Gaussian fittings to both spectra are shown in Fig. 2f. The noisy spectra show that finding peak positions from single frames by fitting is not ideal, and hence why, in this work, the peak positions are calculated using eq. (S3). Fig. 2d represents the histograms of spectral peak positions from the blinking ‘on’ states in Fig. 2b for  $V_{on}$  and  $V_{off}$  frames respectively. Fittings the two histograms to Gaussian functions show

that the centers of the two histograms are separated by 7.5 nm, consistent with the peak shift found in the averaged spectra. The clear separation between the two histograms of peak positions from single  $V_{on}$  and  $V_{off}$  frames also show that the spectral shift can be detected from single frames without averaging. The histograms for average  $\Delta F/F$  and  $\Delta\lambda$  calculated from single particles as described above for all the NPs listed in table 1 are shown in Fig. S5-3.

As seen in Fig. 2, the fluorescence from single NP exhibited intermittency (blinking) as well as changes by the voltage modulations. In the blinking ‘off’ states, no fluorescence and hence no fluorescence modulation by the applied voltage can be observed. In the blinking ‘on’ states, however, there is a wide distribution in fluorescence intensity ( $F$ ) and wavelength ( $\lambda$ ) even in the absence of voltage (see Fig. 2a and 2b for examples), which result in variations in the percent intensity change ( $\Delta F/F$ ) and the spectral shifts ( $\Delta\lambda$ ) by voltage modulation between different modulation periods. For all NPs,  $\Delta\lambda$  and  $\Delta F/F$  are often not constant throughout the acquisition period but rather appears as “bursts” of large responses following periods of small or noisy responses. Moreover, averaging the  $\Delta\lambda$  and  $\Delta F/F$  from only blinking ‘on’ states requires introducing a blinking threshold, which inevitably creates bias when the ‘on’ and ‘off’ states are not clearly separated as shown in Fig. 2a and Fig. S5-2a. Therefore, a burst searching algorithm was applied for each NP time trace to extract the  $\Delta F/F$  or  $\Delta\lambda$  from time trace windows of 8 or more consecutive frames with  $\Delta F/F$  or  $\Delta\lambda$  above a set threshold. Details for the burst search algorithm are given in SI-5. Briefly, the  $|\Delta F/F|^2$  and the  $|\Delta\lambda|^2$  trace were first calculated between neighboring frames, resulting in the “score<sup>2</sup>” trace to be used for burst searching. A “start” of a “burst” was identified when the  $|\Delta F/F|^2$  or  $|\Delta\lambda|^2$  was larger than the score threshold, defined as

the 50% percentiles of the moving averaged “score<sup>2</sup>” trace with a window of 8 frames. A burst “stopped” when the averaged “score<sup>2</sup>” dropped below the threshold. If a burst lasted more than 8 consecutive frames (time

NP compositions	Band diagram	TEM image	NP compositions	Band diagram	TEM image
(i) Type-I CdSe/ZnS 6 nm QDs			(iv) Quasi-type-I CdSe/CdS 40 nm NRs		
(ii) Quasi-type-I CdS/CdSe/CdS 12 nm QDs			(v) Type-II ZnSe/CdS 12 nm NRs		
(iii) Quasi-type-I Te-doped CdSe/CdS 40 nm NRs					

**Table 1.** Composition, band diagram and TEM images of NPs investigated in this study.

threshold), the “start”, “stop”, and “score” (mean of  $\Delta\lambda$  or  $\Delta F/F$ ) of this burst would be recorded. The correlation between the  $\Delta\lambda$  and  $\Delta F/F$  (as discussed below) were small, therefore the burst search was applied separately to  $\Delta\lambda$  and  $\Delta F/F$  traces. Example  $\Delta F/F$  and  $\Delta\lambda$  traces with identified bursts are shown in Figs. S5-5 and S5-6, respectively. After applying the burst search algorithm to all traces from all NPs, the histograms of  $\Delta\lambda$  and  $\Delta F/F$  of individual “bursts” per NP type are plotted in Fig. 3.

### 2.3. Single-particle QCSE results

With the setup and analysis for high-throughput QCSE measurements described above, we measured QCSE responses of 5 different types of NPs and build single-particle histograms to compare the voltage sensitivities,  $\Delta\lambda$  and  $\Delta F/F$ , between NPs with different shapes, sizes and band alignments. Table 1 summarizes the properties of the NPs measured in this work, including: (i) 6 nm type-I CdSe/ZnS QDs; (ii) 12 nm quasi-type-I CdS/CdSe/CdS QDs<sup>48</sup>; (iii) 40 nm quasi-type-I Te-doped CdSe/CdS NRs; (iv) 40 nm quasi-type-I CdSe/CdS NRs; and (v) 12 nm type-II ZnSe/CdS NRs. Fig. 3 shows the histogram of single-particle voltage sensitivities (averaged  $\Delta\lambda$

and  $\Delta F/F$  from individual “bursts”) measured from these samples. Sample (i) is the typical type-I QDs that are commercially available, in which both the excited hole and electron reside in the CdSe core. Sample (ii) is a core-shell-shell spherical QD, in which the excited hole resides in a shell shaped quantum well in the CdSe layer, and the excited electron delocalizes across the entire QD. This QD was reported to have suppressed blinking and near-unity QY<sup>48</sup>. Sample (iii) and (iv) are quasi-type-I NRs with and without Te doping in the CdSe core, which forms a trap for excited holes<sup>49</sup>. The Te-doped 40 nm CdSe/CdS NRs (sample (iii)) have on average 1 atom of Te in the CdSe core.

QCSE responses of type-I and type-II NPs are clearly distinct as shown in Fig. 3. Type-I QDs exhibit mostly red shifts under electric field (samples (i) - (iv) in Fig. 3a) while 47 % of bursts from type-II NRs exhibit blue shifts and 53 % exhibit red shifts (samples (v), dashed line in Fig. 3a). Type-I QDs exhibit very small negative  $\Delta F/F$  (samples (i) in Fig. 3b), i.e., they decrease in intensity under electric field, while 43 % of bursts from type-II NRs exhibit positive  $\Delta F/F$  and 57 % exhibit negative  $\Delta F/F$  (samples (v), dashed line in Fig. 3b). We note here that

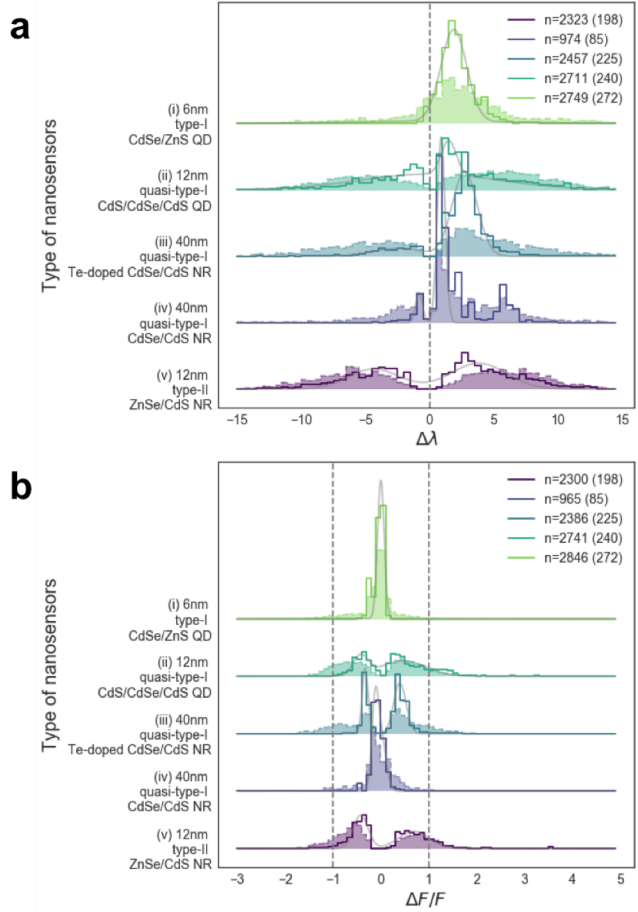


**Fig. 3:** Histograms of (a)  $\Delta\lambda$  and (b)  $\Delta F/F$  extracted from bursts from 5 types of NPs described in Table 1. The number of bursts (n) and number of NPs (number in parenthesis) in each histogram are shown in the legends. The solid lines are the histogram weighted by the total intensity counts during each burst, and the shaded areas with dashed lines are the histogram without any weight. Type-II NRs exhibit the largest voltage sensitivities, with positive and negative  $\Delta F/F$  and  $\Delta\lambda$  responses. The gray lines show the fitting of the distributions to two Gaussians.

in the case of decreased intensity by voltage modulation, the intensity counts can only decrease to 0 in theory, i.e.  $\Delta F/F$  has a lower bound of -1. The bursts that showed  $\Delta F/F < -1$  (4.7 % of bursts from type-II NR, dashed line in Fig. 3b) were due to the events with extremely low counts after background subtraction and the occasional fluctuation of a portion of the intensity traces below 0. The  $\Delta F/F$  traces within these events were often noisy, and the averaged  $\Delta F/F$  could be close to -1 due to the low intensity counts in both  $V_{on}$  and  $V_{off}$  frames. Therefore, to avoid these events from misrepresenting the distributions of  $\Delta F/F$ 's and  $\Delta\lambda$ 's, the histograms of both  $\Delta F/F$  and  $\Delta\lambda$  bursts weighted by the total intensity counts within the bursts were calculated and plotted in Fig. 3. The bursts with higher intensity counts also had higher statistical significance, and hence weighting by total intensity counts was chosen. The weighted histograms show almost no population with  $\Delta F/F$ 's  $< 1$ , attesting that the major cause of the population with  $\Delta F/F$ 's  $< -1$  is as discussed above. By fitting the weighted  $\Delta\lambda$  distributions with two Gaussians, two populations centering at  $-4.3 \text{ nm} \pm 2.0 \text{ nm}$  (1 sigma from Gaussian fitting) and  $3.8 \text{ nm} \pm 2.2 \text{ nm}$  were found for type-II NRs (sample (v)), and only one major population centering at  $1.9 \text{ nm} \pm 1.0 \text{ nm}$  was found for type-I QDs (sample (i)) (gray lines in Fig. 3a). For  $\Delta F/F$  distributions, fitting the weighted  $\Delta F/F$  histograms with two Gaussians yielded two populations centering at  $69\% \pm 32\%$  and  $-42\% \pm 16\%$  for type-II NRs (sample (v)) and only one population centering at  $0\% \pm 7\%$  for type-I QDs (sample (i)) (gray lines in Fig. 3b). In Fig. 3, the number of bursts and number of NPs from which the bursts were extracted are shown in the legends. The average width of bursts, average number of bursts per particle, and percent burst duration as compared to the entire course of acquisitions are shown in Fig. S5-7. The effect of time threshold, defining the minimal burst width, on the distributions of  $\Delta F/F$  and  $\Delta\lambda$  was also studies and shown in Fig. S5-8. The distributions of  $\Delta F/F$  and  $\Delta\lambda$  are not affected by the time threshold from 8 frames to 16 frames, and for both positive and negative  $\Delta F/F$  and  $\Delta\lambda$ , the absolute

values of  $\Delta F/F$  and  $\Delta\lambda$  from bursts decreases as the time threshold increases to 64 frames due to averaging.

To assess the degree of correlation between  $\Delta F/F$  and  $\Delta\lambda$ , a single 2-dimensional histogram of  $\Delta F/F$ 's and  $\Delta\lambda$ 's was plotted using 125 individual type-II NRs (sample(v)) each contributing  $\sim 450$  modulation cycles on average (Fig. 4a). For type-II NRs, the correlation between  $\Delta F/F$ 's and  $\Delta\lambda$ 's was very small, as shown by the Pearson's correlation coefficient (-0.083) (Fig. 4a). The same small correlation was also found between averaged  $\Delta F/F$  and  $\Delta\lambda$  from individual NRs (Fig. S5-4). Similarly,  $\Delta F/F$ - $\Delta\lambda$  Pearson's correlation coefficients were calculated for all types of NPs studied here and the results are shown in Fig. 4b. The distributions of the correlation coefficients (green) are compared to those calculated from the same  $\Delta F/F$  trace and 10 randomly shuffled  $\Delta\lambda$  traces (pink; shuffling procedure described in SI-5 and Fig. S5-9). The shuffling procedure was repeated 10 times to generate 10 distributions of Pearson's correlation coefficients for each NP type (as a negative control, to be compare with the original distributions). The results show that 56% of type-II NRs (111 NRs out of 198 NRs) were negatively correlated while 20% were

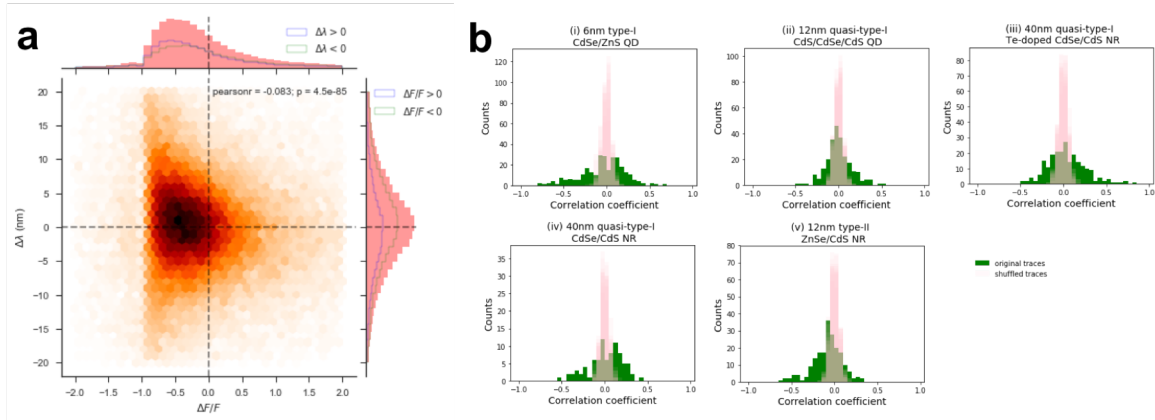


**Fig. 4:** (a) 2D histogram of  $\Delta F/F$  and  $\Delta\lambda$  constructed from each modulation cycles from 125 type-II ZnSe/CdS NRs (sample (v)) including blinking 'off' states. The distributions of  $\Delta F/F$  and  $\Delta\lambda$  are shown on the top and right panel, respectively. Within the top (or the right) panel, the histograms of sub-populations,  $\Delta\lambda$  (or  $\Delta F/F$ )  $> 0$  and  $\Delta\lambda$  (or  $\Delta F/F$ )  $< 0$ , are plotted with the blue and the green lines, respectively. (b) Histograms of Pearson's correlation coefficients extracted from individual NPs for each type of NP (green). The distributions are compared to the distributions of Pearson's correlation coefficients calculated between the same  $\Delta F/F$  traces and 10 randomly shuffled  $\Delta\lambda$  traces (pink, serving as controls).

positively correlated with the correlation coefficients at least one standard deviation away from the mean of the controls' correlation coefficients. For type-I QDs, 43% (117 QDs out of 272 QDs) were negatively correlated while 40% were positively correlated. The results show that for the majority of NPs, the  $\Delta F/F$  and  $\Delta\lambda$  were correlated. However, for some NPs, the correlation coefficients could be positive instead of negative, opposing the prediction by the theory of QCSE.

#### 2.4. Temporal response of single type-II ZnSe/CdS NRs

To capture an AP, a membrane voltage sensor needs to have a sub-ms temporal response and a photon emission rate which allows recording it with sufficient signal-to-noise ratio (SNR). In principle, the response time of NRs is on the order of their excited state lifetime, which is of the order of a few tens of nanoseconds. Bar-Elli *et al.* have shown that bright NRs (with photon emission rate of  $\sim 10^5$  Hz) could report voltage at 1kHz via their spectral shifts,  $\Delta\lambda$ 's<sup>50</sup>. Here we set up to directly resolve the fluorescence intensity of individual NRs in response to voltage modulations with a custom wide-field photon counting camera (PCC) designed for time-resolved single-molecule imaging<sup>51-55</sup>.

For this experiment, we deposited NRs in between lithographically patterned horizontal

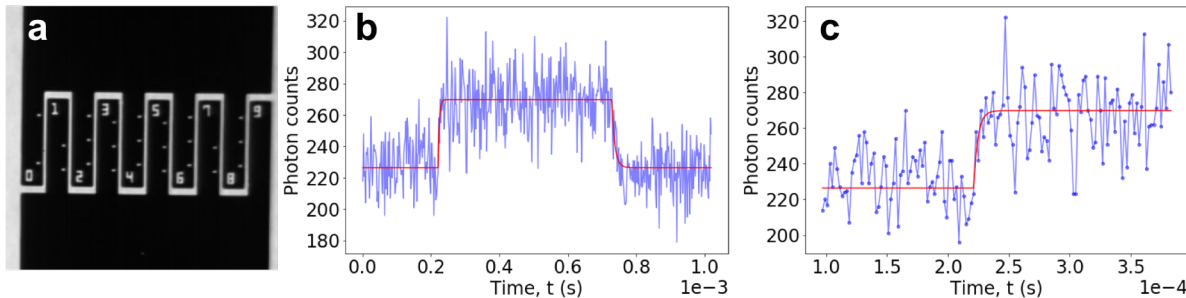


**Fig. 5:** Temporal response of a single NR. (a) An image of the lithographically patterned microelectrode (with 2  $\mu\text{m}$  gap) used in this experiment. (b) Accumulated photon counts from one single NR (from an acquisition of 276 seconds, blue) as a function of photon arrival time with respect to the voltage trigger. The time bin is 2  $\mu\text{s}$ , and the modulation frequency was 1 kHz. The red line is a fit to the photon count trace with equation (1) to extract time constants. (c) Zoom-in to the rising edge in (b), from which the fit (red line) yields a response time of 3.5  $\mu\text{s}$ .

microelectrodes<sup>11</sup> with a 2  $\mu\text{m}$  gap (Fig. 5a) and imaged them with the PCC while applying a

modulated voltage on the electrodes. In contrast to conventional cameras which accumulate photoelectrons generated during a preset integration time, readout the whole frame at fixed interval, and suffer from readout noise, the PCC records each photon's arrival times with a 156 ps temporal resolution, and its location with 50  $\mu$ m spatial resolution, allowing to define arbitrary “frame” durations post acquisition and be readout noise-free. The maximum practical frame rate is only limited by the signal, which is itself limited by detector hardware constraints. In the device used for these experiments, local (single NR) count rate was limited to  $\sim$ 40 kHz, while the global count rate (full detector) was limited to  $\sim$ 2 MHz. In addition, for periodic processes such as studied here, the availability of precise photon timing allows for accumulation of data from “frames” of duration much shorter than the above limits, the signal being now limited only by the total acquisition time. This allowed us to define frame rates comparable to the fastest complementary metal oxide semiconductor (CMOS) cameras but with single-photon sensitivity due to the absence of readout noise.

Type-II NRs in toluene were drop casted on the microelectrodes and covered with polyvinylpyrrolidone (PVP) by spin-coating after toluene evaporation. During the acquisition of photons by the PCC, 1 kHz square voltage modulation (at 50% duty cycle) was applied to create alternating electric fields alternating between 0 and 400 kV/cm. The triggers for the voltage modulations were simultaneously recorded by the PCC electronics and time stamped with an internal 50 MHz clock synchronized with that used to time-stamp detected photons. 269,904 modulation periods were recorded for the single-particle intensity time trace shown in Fig. 5b. Fig. 5a shows the electrodes used for this experiment. Fig. 5b shows the accumulated photon counts after reassignment to a single modulation period. The  $\Delta F/F$  of this specific NR was calculated to be 19%.

To extract the temporal response of the NRs, we fitted the signals with the following equation:

$$\begin{aligned}
 F(t < \mu_1) &= F_0 \\
 F(\mu_1 < t < \mu_2) &= \Delta F \left( 1 - e^{-\frac{t-\mu_1}{\tau_1}} \right) + F_0 \\
 F(t > \mu_2) &= \Delta F \left( e^{-\frac{t-\mu_2}{\tau_2}} \right) + F_0 \quad \text{eq. (3)}
 \end{aligned}$$

where  $F$  is the photon counts, which is a function of time,  $t$ .  $\mu_1$  and  $\mu_2$  are fitted parameters for the time when the NR's intensity rises and decays, respectively.  $\tau_1$  and  $\tau_2$  are fitted parameters for the rise and decay time constant, respectively.  $F_0$  represents the total photon counts in the absence of voltage, and  $\Delta F$  is the change in photon counts under applied voltage as compared to  $F_0$ . Therefore,  $\Delta F/F$  equals  $\Delta F / F_0$ . Fitting the accumulated trace to eq. (3) yielded a time constant  $\tau_1 = 3.5 \mu\text{s}$  (Fig. 5c) for the rising edge, which is exactly the rise time of the measuring circuit (including the voltage amplifier and RC time constant of the microelectrodes, Figs. S6-1 and S6-2). The measured response time is therefore an upper bound imposed by the instrument, and is  $\sim 30$  times faster than what is needed to resolve an AP. We note that although the excitation power and excitation wavelength were not tuned to achieve the largest possible emission rate, single NRs exhibited  $> 4$  kHz emission rate. Improvement in the quantum yield (QY) of NRs and using a stronger excitation to increase the emission rate to  $\sim 30$  kHz ( $\sim x 7$  fold increase) will be needed to overcome shot noise in order to record a single AP at 1 kHz.

### 3. Discussion:

*In vitro* QCSE screening results have shown wide distributions of voltage sensitivities ( $\Delta F/F$  and  $\Delta\lambda$ ) for single NRs from the best batch of type-II ZnSe/CdS NRs (sample(v)). Some

NRs exhibited large spectral shifts (red shifts or blue shifts), while some exhibited small or no spectral shifts. Some NRs exhibited large changes (positive or negative) in emission intensity ( $\Delta F/F$ ), while some exhibited small or no changes in  $\Delta F/F$ . Since we did not attempt to align the NRs along the electric field direction, and since the synthesis itself presents some degree of heterogeneity (in sizes, shape, and quantum yields) among particles, the heterogeneity in voltage responses is expected. Due to the random orientation of NR with respect to the applied electric field, both red shifts and blue shifts as well as positive and negative  $\Delta F/F$  under applied electric field were observed from the type-II NRs. These phenomena are predicted by theory<sup>13</sup> and attest to the type-II nature of these NRs and their asymmetric structure, in which excited carriers separate to form a dipole that partially screens the external electric field. Comparing type-II NRs to type-I spherical QDs, in which the excited dipole is small and isotropic due to quantum confinement in the spherical core (well), type-II NRs exhibit  $\Delta F/F$  and  $\Delta\lambda$  with both signs (positive and negative) as well as larger absolute values of  $\Delta F/F$  and  $\Delta\lambda$  under both signs. The results by burst search (Fig. 3) and by comparing the  $\Delta\lambda$  distributions with that from randomized wavelength ( $\lambda$ ) traces (Fig. S5-9) both show that type-II NRs exhibit  $\Delta\lambda$  of both signs while type-I QDs and quasi-type-I NRs exhibit primarily positive  $\Delta\lambda$ 's. For type-II NRs, despite some heterogeneity, the average  $\Delta F/F$  in Fig. 3 is very large (69% for positive  $\Delta F/F$  and -42% for negative  $\Delta F/F$ ), and the average  $\Delta\lambda$  for the red-shifted and blue-shifted populations are +3.8 nm and -4.3 nm, respectively for an electric field of 400 kV/cm, which is approximately 1.45 times larger than the electric field swing that will be created during firing of an AP in a neuron. The  $\Delta F/F$  from the type-II NRs, even when divided by a factor of 1.45, is much larger than most commercially available VSDs (di-8-ANEPPS: 7.5% per 100 mV<sup>56</sup>; di-4-ANEPPS: 4.13% at 560 nm and 2.12% at 620 nm per 150 mV<sup>57</sup>; RH237: 2-3 %<sup>58</sup>; JPW-6003: 11.9%<sup>59</sup>) or GEVIs and has much higher signal-to-background ratio at the single

particle level. However, we note that according to the theoretical studies by Park *et. al*<sup>60</sup>,  $\Delta F/F$  is dependent on the QY of the NP as well as on the excitation power (which in turn affects the QY via re-partitioning between the exciton state and the positive trion state). For a 12 nm type-II ZnSe/CdS NR with 10% QY and 100% partitioning in the exciton state,  $\Delta F/F$  is estimated to be  $> 60\%$ , while the same NR with 90% QY and 20% partitioning in the exciton state exhibits a  $\Delta F/F$  of only  $\sim 5\%$ <sup>13</sup>. While a larger QY and larger excitation power could allow a higher emission rate, they also decrease  $\Delta F/F$  and the partitioning in the exciton state. A careful balancing of the trade-off between  $\Delta F/F$ , QY and excitation power is therefore needed in order to achieve AP recordings. As reported by Park *et al.*, the  $\Delta F/F$  caused by the intrinsic QCSE effect without considering defect or charge trapping states would only result in a negative correlation between the  $\Delta\lambda$  and  $\Delta F/F$ . However, all the NPs studied in this work showed a population with positively correlated  $\Delta\lambda$  and  $\Delta F/F$ . The reasons for positively correlated  $\Delta\lambda$  and  $\Delta F/F$  could be that  $\Delta F/F$  was induced by a combined result of the applied electric field and local charges at surface and interface defects<sup>61</sup> since local charge states can create a local electric field<sup>10</sup> and be modulated by the applied electric field<sup>62</sup>. Fig. S5-4 shows that for single type-II NRs, the  $\Delta\lambda$ 's and  $\Delta F/F$ 's obtained from averaging all the blinking 'on' states over multiple modulation cycles are only weakly correlated as expected from a polydispersed population of NRs.  $\Delta\lambda$ 's and  $\Delta F/F$ 's were found to be correlated when the analyses were performed for individual NPs (Fig. 4b). A pure (intrinsic) QCSE predicts negative correlation between  $\Delta\lambda$  and  $\Delta F/F$ . However, extrinsic charging/ionization at surface- and interface-defects<sup>62</sup> could further modulate blinking rates (and hence QY) and contribute to a positive correlation and/or no correlation. These effects will require further studies that correlate spectral, intensity and lifetime measurements under applied electric field and at different excitation powers (currently a topic of a follow-up project). Such measurements will allow us to decouple these

contributions and further improve type-II NRs as voltage sensors (for example, by growing an additional layer of a high bandgap coat). Indeed, the high-throughput screening method developed in this work is most suitable and will be used to minimize extrinsic effects and optimize the intrinsic QCSE signal.

Furthermore, the large  $\Delta\lambda$  shift from the type-II NRs (relative to their emission spectral width) is amenable to ratiometric detection using a dual-channel spectral splitting setup<sup>11, 50</sup>. Together with further improvements in the sensors' design and performance and in their surface functionalization for membrane insertion<sup>14</sup>, we envision their utilization for parallel, multi-site, super-resolved electrophysiological recordings.

## METHODS

Materials and chemicals: All chemicals are used as purchased without further purification. Trioctylphosphine oxide (TOPO, 99%), Octadecylphosphonic acid (ODPA) and hexylphosphonic acid (HPA) were purchased from PCI Synthesis. Tri-n-octylphosphine (TOP, 97%) was obtained from Strem Chemicals. Cadmium oxide (CdO), octadecylamine (ODA), hexadecylamine (HDA), octadecanethiol (ODT), 1.0 M diethylzinc ( $Zn(Et)_2$ ) solution in hexanes, were purchased from Sigma-Aldrich. Selenium powder (99.999%, 200 mesh) was purchased from Alfa Aesar.

Synthesis of ZnSe/CdS NRs: The detailed procedure for synthesis of ZnSe QDs is described in Dorfs et al<sup>44</sup>. Briefly, a mixture of Se (63 mg), TOP (2 g) and diethyl zinc solution (0.8 ml, 1M) was injected into degassed HDA (7 g) at 300 °C in argon atmosphere. The reaction was kept at 265 °C until a sharp absorption peak around 360 nm was observed (~30 mins after injection). After the reaction was cooled to room temperature, ZnSe QDs were purified 3 times by butanol/methanol

precipitation and redissolved in toluene. The concentration of ZnSe in toluene was documented by the optical density (OD) at the absorption peak through a 1 cm cuvette. To synthesize CdS nanorods on ZnSe seeds using WANDA, CdO (270 mg), ODPA (1305 mg), HPA (360 mg), and TOPO (13.5 g) were first degassed at 100 °C under vacuum for 2 hr, and the solution was heated to 230 °C until the CdO powder was fully dissolved, rendering a colorless solution. The solution was cooled to, room temperature to add 180 mg ODA, and the solution was degassed under vacuum at 100 °C for additional 2 hr. To prepare the S precursor solution with ZnSe, 1440 mg of ODT were mixed with 36 units [OD (under 1cm path length) × ml] of ZnSe solution in toluene and heated under vacuum to remove the toluene and moisture. After degassing, both Cd precursor solution and S precursor with ZnSe were transferred under vacuum into a glove box and dispensed gravimetrically into the 40 ml glass vials used as reaction vessels for the robot. The filled vials were loaded into the eight-reactor array of WANDA, an automated nanocrystal synthesis robot at the Molecular Foundry<sup>46</sup>. WANDA was used to run up to eight reactions in serial with individually controlled heating/cooling profiles, stirring rate, injections and aliquot schedules. Below is the description of an exemplary run. 1.133 ml of S/ZnSe solution (heated to 50 °C to prevent solidification) was injected into 15615 mg of Cd solution at 330 °C at a dispense rate of 1.5 ml/sec. The temperature after injection was set at 320 °C for CdS NR growth. The heating was stopped 15 mins after injection. To thermally quench the reaction, each reaction was then rapidly cooled to 50 °C using a stream of nitrogen, after which 5 ml of acetone was injected.

*Post-synthesis treatment of ZnSe/CdS NR:* The obtained product was purified 3 times by methanol precipitation and toluene wash/centrifugation to remove free ligands and unreacted precursors, and a half monolayer of Zn was grown on the NRs' surface to introduce metal rich surface and coordinating ligands for further functionalization while maintaining QY (30-40%) of these NRs

during and after functionalization. Briefly, the purified ZnSe/CdS NRs were mixed with TOPO, oleic acid and oleylamine. Following degassing, the reaction solution was heated to 250-280°C under argon, a TOP solution of zinc acetate or zinc undecylenate was infused to the reaction flask with a needle mounted syringe. The reaction was stopped by removing the heating mantle 20 min later.

*Wide field spectrally resolved microscopy for QCSE measurements:* A wide field microscope based on Zeiss Axiovert S100TV, with home-built illumination and detection optics, was used. A 460 nm laser (Sapphire 460-10, Coherent) was focused onto the back focal plane of a 100× objective (Zeiss Plan-Neofluar, N.A. 1.3, oil immersion) to create wide-field illumination. The laser power was 0.7 mW before entering the objective. A 488 nm dichroic mirror (Di03-R488, Semrock) and a 530 nm long pass filter (E530LP, Chroma Technologies) were used. In the detection path, a removable Amici prism could be inserted before the electron-multiplying charged couple device (EMCCD) (Ixon DU-897, Andor) for spectrally dispersing PSFs. For each QCSE measurements, a wide field image without the Amici prism was first acquired to locate each NP. After inserting the prism, a movie was acquired while synchronously alternating the voltage applied to the sandwich device as described below. Alternating voltage between 0 ( $V_{\text{off}}$ ) and  $\sim$ 60 V ( $V_{\text{on}}$ ) (variable depending on the final thickness of  $\text{SiO}_2$ , PVP, and  $\text{SiO}_2$  layer in each device) was generated by a function generator (FG2A, Beckman Industrial) creating square wave at 8 Hz with 50% duty cycle and amplified with an additional offset of  $\sim$ 30 V (variable, to offset the voltage in half periods to 0 V) by a high bandwidth voltage amplifier (STM100, RHK Technology). The exact voltage applied for  $V_{\text{on}}$  was calculated to impose an electric field of 400 kV/cm in the PVP layer, assuming that the two  $\text{SiO}_2$  layers and the one PVP layer were acting as three capacitors in series with dielectric constants of 3.9 and 2.33 for  $\text{SiO}_2$  and PVP, respectively.

Synchronization of the function generator and the EMCCD camera was achieved by a programmable FPGA board (410-087, Digilent Inc.), which identified downward and upward zero voltage crossings from the voltage generator and output TTL triggers at each crossing. As a result, two frames were recorded for each modulation period (one frame with voltage on, one frame with voltage off). Therefore, the resulted exposure time for each frame was 62.5 ms, and the frame rate was 16 Hz. All movies consisted of 600 frames. The algorithms for extracting QCSE parameters from these movies is described briefly below and in detail in SI-5.

*Wide-field photon counting microscopy using a photon-counting camera:* An inverted wide field microscope based on Olympus IX71 with home-built excitation and detection optics was constructed. The excitation source was 532 nm continuous wave laser (MGL-III-532-150mW, Opto Engine). The laser was reflected by a 488/532 long pass dichroic mirror (Omega Optical, transmission spectrum shown in SI-7) and focused onto the back focal plane of a 60 $\times$  objective with a numerical aperture (N.A.) of 1.45 (Plan Apo TIRFM, Olympus) to create wide field illumination. The excitation power was 1.9 mW before entering the objective. A 596/60 band pass filter (596DF60, Omega Optical) was used as the emission filter. Details for the hardware and software for the photon-counting camera (PCC) are similar to those presented in Colyer *et al*<sup>55</sup> with the following differences: the detector was comprised of a GaAs photocathode with quantum efficiency of ~30% in the detection wavelength range and a cross-strip anode for position sensing<sup>63</sup>. Dilute NR solution in toluene were drop-casted onto lithographically patterned electrodes, allowed to dry in air, and covered with a layer of PVP by spin-coating. After locating NRs in between the electrodes under microscope, square wave voltage was applied via the same hardware used for QCSE measurements, while the emitted photons from NRs were detected and time-stamped by the PCC. Since the detector does not accumulate photons into “frames” but

instead collects position and time information for each photon, synchronization of acquired photons was performed with the help of TTL triggers emitted by the voltage function generator, recorded as a separate time-stamped signal by the PCC electronics. Because of hardware limitation, only 1 every 8 trigger signal was recorded, which provided plenty of information for post-acquisition synchronization, each time-stamp being recorded with 20 ns resolution.

*Fabrication of sandwich devices:* An 18 mm x 18 mm indium tin oxide (ITO) coated coverslip (#1.5, 30-60 ohms per square resistivity, SPI Supplies) was used as the starting substrate. 500 nm of a SiO<sub>2</sub> layer was deposited using e-beam evaporation (Mark 40, CHA) at a rate of 1.5 Å/s. The resistance of the substrate after SiO<sub>2</sub> deposition was tested and confirmed to be infinite using a multimeter. QDs or NRs in toluene were spin-coated on top of the SiO<sub>2</sub> layer, followed by spin-coating of 5% w/w poly-vinylpyrrolidone (PVP, 40k Sigma-Aldrich) in 1:1 methanol and H<sub>2</sub>O solution to create a layer of PVP of 400-500 nm (measured by a stylus profilometer, Veeco Dektak 8, Bruker). Next, a second 500 nm SiO<sub>2</sub> layer was deposited on top of the PVP layer for insulation, followed by the second electrode deposition of 5 nm Cr layer (0.1 Å/s) and a 100 nm Au layer (1 Å/s) using e-beam evaporation (Mark 40, CHA). The deposition of the second electrode was through a shadow mask that created six electrodes of 3 mm diameter on each coverslip. The thicknesses of each layer were measured with the stylus profilometer (Veeco Dektak 8, Bruker) after each deposition or spin-coating to assist calculation of the voltage required for QCSE measurements.

## AUTHOR INFORMATION

### **Corresponding Author**

\*Corresponding author. E-mail: [sweiss@chem.ucla.edu](mailto:sweiss@chem.ucla.edu)

## Present Addresses

†If an author's address is different than the one given in the affiliation line, this information may be included here.

## Author Contributions

Y.K. conducted all *in vitro* experiments, analyzed all the data, and wrote the manuscript. J.J.L. and Y.K. synthesized ZnSe/CdS NRs using WANDA. ZnSe QDs were synthesized by J.J.L.. N.M. synthesized the 40nm NRs. X.M. built the optical setup with the PCC with excitation source added by Y.K.. X.M. and Y.K. performed related data analysis. E.C. contributed to NR syntheses and provided training for WANDA operation. D.O. provided 2 types of NRs. S.W. and Y.K. designed the experiments. S.W. and D.O. helped in writing and revising the manuscript. All authors have given approval to the final version of the manuscript.

## ACKNOWLEDGMENT

We would like to thank Antonio Ingargiola and Kyoungwon Park for discussion on data analysis, Max Ho and Wilson Lin for discussion on thin film fabrication, Andrew Wang and Ocean Nanotech LLC for providing the CdSe/ZnS QDs at no cost, and Prof. Wan Ki Bae for providing the CdS/CdSe/CdS QDs. This research was supported by DARPA Fund #D14PC00141, by the European Research Council (ERC) advanced grant NVS #669941, by the Human Frontier Science Program (HFSP) research grant #RGP0061/2015 and by the BER program of the Department of Energy Office of Science, grant # DE-FC03-02ER63421. Work at the Molecular Foundry was supported by the Office of Science, Office of Basic Energy Sciences, of the U.S. Department of Energy under Contract No. DE-AC02-05CH11231.

## REFERENCES

1. Michalet, X.; Pinaud, F. F.; Bentolila, L. A.; Tsay, J. M.; Doose, S.; Li, J. J.; Sundaresan, G.; Wu, A. M.; Gambhir, S. S.; Weiss, S., Quantum Dots for Live Cells, in Vivo Imaging, and Diagnostics. *Science* **2005**, *307* (5709), 538.
2. Wen Shi and Xiaohua Li and Huimin, M., Fluorescent probes and nanoparticles for intracellular sensing of pH values. *Methods and Applications in Fluorescence* **2014**, *2* (4), 042001.
3. Chang, Y.-P.; Pinaud, F.; Antelman, J.; Weiss, S., Tracking bio-molecules in live cells using quantum dots. *Journal of biophotonics* **2008**, *1* (4), 287-298.
4. Bhatia, D.; Arumugam, S.; Nasilowski, M.; Joshi, H.; Wunder, C.; Chambon, V.; Prakash, V.; Grazon, C.; Nadal, B.; Maiti, P. K.; Johannès, L.; Dubertret, B.; Krishnan, Y., Quantum dot-loaded monofunctionalized DNA icosahedra for single-particle tracking of endocytic pathways. *Nature Nanotechnology* **2016**, *11*, 1112.
5. Tanimoto, R.; Hiraiwa, T.; Nakai, Y.; Shindo, Y.; Oka, K.; Hiroi, N.; Funahashi, A., Detection of Temperature Difference in Neuronal Cells. *Scientific Reports* **2016**, *6*, 22071.
6. Xu, J.; Tehrani, K. F.; Kner, P., Multicolor 3D Super-resolution Imaging by Quantum Dot Stochastic Optical Reconstruction Microscopy. *ACS Nano* **2015**, *9* (3), 2917-2925.
7. Yang, X.; Zhanghao, K.; Wang, H.; Liu, Y.; Wang, F.; Zhang, X.; Shi, K.; Gao, J.; Jin, D.; Xi, P., Versatile Application of Fluorescent Quantum Dot Labels in Super-resolution Fluorescence Microscopy. *ACS Photonics* **2016**, *3* (9), 1611-1618.
8. Jiang, X.; Qu, X.; Li, B. Q. In *Thermal mapping with quantum dots in a living cell*, 2016 IEEE 10th International Conference on Nano/Molecular Medicine and Engineering (NANOMED), Oct. 30 2016-Nov. 2 2016; 2016; pp 14-18.
9. Medintz, I. L.; Stewart, M. H.; Trammell, S. A.; Susumu, K.; Delehanty, J. B.; Mei, B. C.; Melinger, J. S.; Blanco-Canosa, J. B.; Dawson, P. E.; Mattoussi, H., Quantum-dot/dopamine bioconjugates function as redox coupled assemblies for in vitro and intracellular pH sensing. *Nature Materials* **2010**, *9*, 676.
10. Empedocles, S. A.; Bawendi, M. G., Quantum-Confined Stark Effect in Single CdSe Nanocrystallite Quantum Dots. *Science* **1997**, *278* (5346), 2114.
11. Park, K.; Deutsch, Z.; Li, J. J.; Oron, D.; Weiss, S., Single Molecule Quantum-Confined Stark Effect Measurements of Semiconductor Nanoparticles at Room Temperature. *ACS Nano* **2012**, *6* (11), 10013-10023.
12. Marshall, J. D.; Schnitzer, M. J., Optical Strategies for Sensing Neuronal Voltage Using Quantum Dots and Other Semiconductor Nanocrystals. *ACS Nano* **2013**, *7* (5), 4601-4609.
13. Park, K.; Weiss, S., Design Rules for Membrane-Embedded Voltage-Sensing Nanoparticles. *Biophysical Journal* **2017**, *112* (4), 703-713.
14. Park, K.; Kuo, Y.; Shvadchak, V.; Ingargiola, A.; Dai, X.; Hsiung, L.; Kim, W.; Zhou, H.; Zou, P.; Levine, A. J.; Li, J.; Weiss, S., Membrane insertion of—and membrane potential sensing by—semiconductor voltage nanosensors: Feasibility demonstration. *Science Advances* **2018**, *4* (1).
15. Nimchinsky, E. A.; Sabatini, B. L.; Svoboda, K., Structure and Function of Dendritic Spines. *Annual Review of Physiology* **2002**, *64* (1), 313-353.

16. Hering, H.; Sheng, M., Dendritic spines : structure, dynamics and regulation. *Nat Rev Neurosci* **2001**, *2* (12), 880-888.

17. Rochefort, N. L.; Konnerth, A., Dendritic spines: from structure to *in vivo* function. *EMBO reports* **2012**, *13* (8), 699.

18. Sala, C.; Segal, M., Dendritic Spines: The Locus of Structural and Functional Plasticity. *Physiological Reviews* **2014**, *94* (1), 141.

19. Rochefort, N. L.; Konnerth, A., Dendritic spines: from structure to *in vivo* function. *EMBO reports* **2012**, *13* (8), 699.

20. Bonhoeffer, T.; Yuste, R., Spine Motility. *Neuron* **2002**, *35* (6), 1019-1027.

21. Yoshihara, Y.; De Roo, M.; Muller, D., Dendritic spine formation and stabilization. *Current Opinion in Neurobiology* **2009**, *19* (2), 146-153.

22. Dailey, M. E.; Smith, S. J., The Dynamics of Dendritic Structure in Developing Hippocampal Slices. *The Journal of Neuroscience* **1996**, *16* (9), 2983.

23. Chemla, S.; Chavane, F., Voltage-sensitive dye imaging: Technique review and models. *Journal of Physiology-Paris* **2010**, *104* (1), 40-50.

24. Fairless, R.; Beck, A.; Kravchenko, M.; Williams, S. K.; Wissenbach, U.; Diem, R.; Cavalie, A., Membrane Potential Measurements of Isolated Neurons Using a Voltage-Sensitive Dye. *PLoS One* **2013**, *8* (3), e58260.

25. Woodford, C. R.; Frady, E. P.; Smith, R. S.; Morey, B.; Canzi, G.; Palida, S. F.; Araneda, R. C.; Kristan, W. B.; Kubiak, C. P.; Miller, E. W.; Tsien, R. Y., Improved PeT Molecules for Optically Sensing Voltage in Neurons. *Journal of the American Chemical Society* **2015**, *137* (5), 1817-1824.

26. Wuskell, J. P.; Boudreau, D.; Wei, M.-d.; Jin, L.; Engl, R.; Chebolu, R.; Bullen, A.; Hoffacker, K. D.; Kerimo, J.; Cohen, L. B.; Zochowski, M. R.; Loew, L. M., Synthesis, spectra, delivery and potentiometric responses of new styryl dyes with extended spectral ranges. *Journal of Neuroscience Methods* **2006**, *151* (2), 200-215.

27. St-Pierre, F.; Chavarha, M.; Lin, M. Z., Designs and sensing mechanisms of genetically encoded fluorescent voltage indicators. *Current Opinion in Chemical Biology* **2015**, *27*, 31-38.

28. Han, Z.; Jin, L.; Platisa, J.; Cohen, L. B.; Baker, B. J.; Pieribone, V. A., Fluorescent Protein Voltage Probes Derived from ArcLight that Respond to Membrane Voltage Changes with Fast Kinetics. *PLoS One* **2013**, *8* (11), e81295.

29. St-Pierre, F.; Marshall, J. D.; Yang, Y.; Gong, Y.; Schnitzer, M. J.; Lin, M. Z., High-fidelity optical reporting of neuronal electrical activity with an ultrafast fluorescent voltage sensor. *Nat Neurosci* **2014**, *17* (6), 884-889.

30. Kulkarni, R. U.; Miller, E. W., Voltage Imaging: Pitfalls and Potential. *Biochemistry* **2017**.

31. Loew, L. M., Design and Use of Organic Voltage Sensitive Dyes. In *Membrane Potential Imaging in the Nervous System: Methods and Applications*, Canepari, M.; Zecevic, D., Eds. Springer New York: New York, NY, 2011; pp 13-23.

32. Peterka, D. S.; Takahashi, H.; Yuste, R., Imaging voltage in neurons. *Neuron* **2011**, *69* (1), 9-21.

33. Gong, Y.; Wagner, M. J.; Zhong Li, J.; Schnitzer, M. J., Imaging neural spiking in brain tissue using FRET-opsin protein voltage sensors. **2014**, *5*, 3674.

34. Gong, Y.; Huang, C.; Li, J. Z.; Grewe, B. F.; Zhang, Y.; Eismann, S.; Schnitzer, M. J., High-speed recording of neural spikes in awake mice and flies with a fluorescent voltage sensor. *Science* **2015**.

35. Barry, J. F.; Turner, M. J.; Schloss, J. M.; Glenn, D. R.; Song, Y.; Lukin, M. D.; Park, H.; Walsworth, R. L., Optical magnetic detection of single-neuron action potentials using quantum defects in diamond. *Proceedings of the National Academy of Sciences* **2016**, *113* (49), 14133-14138.

36. Rowland, C. E.; Susumu, K.; Stewart, M. H.; Oh, E.; Mäkinen, A. J.; O'Shaughnessy, T. J.; Kushto, G.; Wolak, M. A.; Erickson, J. S.; L. Efros, A.; Huston, A. L.; Delehanty, J. B., Electric Field Modulation of Semiconductor Quantum Dot Photoluminescence: Insights Into the Design of Robust Voltage-Sensitive Cellular Imaging Probes. *Nano Letters* **2015**, *15* (10), 6848-6854.

37. Nag, O. K.; Stewart, M. H.; Deschamps, J. R.; Susumu, K.; Oh, E.; Tsytarev, V.; Tang, Q.; Efros, A. L.; Vaxenburg, R.; Black, B. J.; Chen, Y.; O'Shaughnessy, T. J.; North, S. H.; Field, L. D.; Dawson, P. E.; Pancrazio, J. J.; Medintz, I. L.; Chen, Y.; Erzurumlu, R. S.; Huston, A. L.; Delehanty, J. B., Quantum Dot–Peptide–Fullerene Bioconjugates for Visualization of in Vitro and in Vivo Cellular Membrane Potential. *ACS Nano* **2017**, *11* (6), 5598-5613.

38. Bean, B. P., The action potential in mammalian central neurons. *Nat Rev Neurosci* **2007**, *8* (6), 451-465.

39. Connors, B. W.; Gutnick, M. J., Intrinsic firing patterns of diverse neocortical neurons. *Trends in Neurosciences* **1990**, *13* (3), 99-104.

40. Connor, J. A., Neural repetitive firing: a comparative study of membrane properties of crustacean walking leg axons. *Journal of Neurophysiology* **1975**, *38* (4), 922.

41. Tateno, T.; Harsch, A.; Robinson, H. P. C., Threshold Firing Frequency–Current Relationships of Neurons in Rat Somatosensory Cortex: Type 1 and Type 2 Dynamics. *Journal of Neurophysiology* **2004**, *92* (4), 2283.

42. Zhou, F. M.; Hablitz, J. J., Layer I neurons of rat neocortex. I. Action potential and repetitive firing properties. *Journal of Neurophysiology* **1996**, *76* (2), 651.

43. Descalzo, V. F.; Nowak, L. G.; Brumberg, J. C.; McCormick, D. A.; Sanchez-Vives, M. V., Slow Adaptation in Fast-Spiking Neurons of Visual Cortex. *Journal of Neurophysiology* **2005**, *93* (2), 1111.

44. Dorfs, D.; Salant, A.; Popov, I.; Banin, U., ZnSe Quantum Dots Within CdS Nanorods: A Seeded-Growth Type-II System. *Small* **2008**, *4* (9), 1319-1323.

45. Hewa-Kasakarage, N. N.; Kiranova, M.; Nemchinov, A.; Schmall, N.; El-Khoury, P. Z.; Tarnovsky, A. N.; Zamkov, M., Radiative Recombination of Spatially Extended Excitons in (ZnSe/CdS)/CdS Heterostructured Nanorods. *Journal of the American Chemical Society* **2009**, *131* (3), 1328-1334.

46. Chan, E. M.; Xu, C.; Mao, A. W.; Han, G.; Owen, J. S.; Cohen, B. E.; Milliron, D. J., Reproducible, High-Throughput Synthesis of Colloidal Nanocrystals for Optimization in Multidimensional Parameter Space. *Nano Letters* **2010**, *10* (5), 1874-1885.

47. Zhang, Z.; Kenny, S. J.; Hauser, M.; Li, W.; Xu, K., Ultrahigh-throughput single-molecule spectroscopy and spectrally resolved super-resolution microscopy. *Nat Meth* **2015**, *12* (10), 935-938.

48. Jeong, B. G.; Park, Y.-S.; Chang, J. H.; Cho, I.; Kim, J. K.; Kim, H.; Char, K.; Cho, J.; Klimov, V. I.; Park, P.; Lee, D. C.; Bae, W. K., Colloidal Spherical Quantum Wells with Near-Unity Photoluminescence Quantum Yield and Suppressed Blinking. *ACS Nano* **2016**, *10* (10), 9297-9305.

49. Meir, N.; Martín-García, B.; Moreels, I.; Oron, D., Revisiting the Anion Framework Conservation in Cation Exchange Processes. *Chemistry of Materials* **2016**, *28* (21), 7872-7877.

50. Bar-Elli, O.; Steinitz, D.; Yang, G.; Tenne, R.; Ludwig, A.; Kuo, Y.; Triller, A.; Weiss, S.; Oron, D., Shot noise limited voltage sensing with single nanorods via the quantum confined Stark effect. *Unpublished*.

51. Michalet, X.; Colyer, R. A.; Scalia, G.; Weiss, S.; Siegmund, O. H. W.; Tremsin, A. S.; Vallerga, J. V.; Villa, F.; Guerrieri, F.; Rech, I.; Gulinatti, A.; Tisa, S.; Zappa, F.; Ghioni, M.; Cova, S., New photon-counting detectors for single-molecule fluorescence spectroscopy and imaging. *Proceedings of SPIE* **2011**, 8033, 803316.

52. Michalet, X.; Colyer, R. A.; Antelman, J.; Siegmund, O. H. W.; Tremsin, A.; Vallerga, J. V.; Weiss, S., Single-quantum dot imaging with a photon counting camera. *Current pharmaceutical biotechnology* **2009**, 10 (5), 543-558.

53. Tremsin, A. S.; Siegmund, O. H. W.; Vallerga, J. V.; Raffanti, R.; Weiss, S.; Michalet, X., High Speed Multichannel Charge Sensitive Data Acquisition System with Self-Triggered Event Timing. *IEEE transactions on nuclear science* **2009**, 56 (3), 1148-1152.

54. Michalet, X.; Siegmund, O. H. W.; Vallerga, J. V.; Jelinsky, P.; Millaud, J. E.; Weiss, S., Photon-Counting H33D Detector for Biological Fluorescence Imaging. *Nuclear instruments & methods in physics research. Section A, Accelerators, spectrometers, detectors and associated equipment* **2006**, 567 (1), 133-133.

55. Colyer, R. A.; Siegmund, O. H. W.; Tremsin, A. S.; Vallerga, J. V.; Weiss, S.; Michalet, X., Phasor imaging with a widefield photon-counting detector. *Journal of Biomedical Optics* **2012**, 17 (1), 016008.

56. Hardy, M. E. L.; Lawrence, C. L.; Standen, N. B.; Rodrigo, G. C., Can optical recordings of membrane potential be used to screen for drug-induced action potential prolongation in single cardiac myocytes? *Journal of Pharmacological and Toxicological Methods* **2006**, 54 (2), 173-182.

57. Kao, W. Y.; Davis, C. E.; Kim, Y. I.; Beach, J. M., Fluorescence Emission Spectral Shift Measurements of Membrane Potential in Single Cells. *Biophysical Journal* **2001**, 81 (2), 1163-1170.

58. Choi, B.-R.; Salama, G., Simultaneous maps of optical action potentials and calcium transients in guinea-pig hearts: mechanisms underlying concordant alternans. *The Journal of Physiology* **2000**, 529 (Pt 1), 171-188.

59. Matiukas, A.; Mitrea, B. G.; Qin, M.; Pertsov, A. M.; Shvedko, A. G.; Warren, M. D.; Zaitsev, A. V.; Wuskell, J. P.; Wei, M.-d.; Watras, J.; Loew, L. M., Near-infrared voltage-sensitive fluorescent dyes optimized for optical mapping in blood-perfused myocardium. *Heart Rhythm* **2007**, 4 (11), 1441-1451.

60. Park, K.; Weiss, S., Performance Predictions and Design Rules for Membrane-Embedded Semiconducting Voltage-Sensing Nanoparticles. *Biophysical Journal* **2016**.

61. Yuan , G.; Gomez , D.; Kirkwood, N.; Boldt, K.; Mulvaney, P., Two Mechanisms Determine Quantum Dot Blinking. *ChemRxiv*: 2017.

62. Park, S.-J.; Link, S.; Miller, W. L.; Gesquiere, A.; Barbara, P. F., Effect of electric field on the photoluminescence intensity of single CdSe nanocrystals. *Chemical Physics* **2007**, 341 (1), 169-174.

63. Siegmund, O.; Vallerga, J.; Tremsin, A.; McPhate, J.; Michalet, X.; Weiss, S.; Frisch, H.; Wagner, R.; Mane, A.; Elam, J.; Varner, G., Large Area and High Efficiency Photon Counting Imaging Detectors with High Time and Spatial Resolution for Night Time Sensing and Astronomy. In *Advanced Maui Optical and Space Surveillance Technologies Conference*, Maui, HI, 2012.

